ACS OMEGA

Open Access

http://pubs.acs.org/journal/acsodf

Article

Visible Light-Driven Photocatalytic Degradation of Methylene Blue Dye Using a Highly Efficient Mg−Al LDH@g-C_3N_4@Ag_3PO_4 Nanocomposite

Ghazal Salehi, Mojtaba Bagherzadeh,* Reza Abazari, Mojtaba Hajilo, and Davood Taherinia

Cite This: *ACS Omega* 2024, 9, 4581−4593

Read Online

ACCESS | Metrics & More | Article Recommendations | Supporting Information

ABSTRACT: The issue of water resource pollution resulting from the discharge of dyes is a matter of great concern for the environment. In this investigation, a new ternary heterogeneous Mg−Al LDH@g-C_3N_4X@Ag_3PO_4Y (X = wt % of g-C_3N_4 with respect to Mg−Al layered double hydroxide (LDH) and Y = wt % of Ag_3PO_4 loaded on Mg−Al LDH@g-$C_3N_4$30) nanocomposite was prepared with the aim of increasing charge carrier separation and enhancement of photocatalytic performance to degrade methylene blue (MB) dye. The prepared samples were subjected to characterization via Fourier-transform infrared spectroscopy, field emission scanning electron microscopy, energy-dispersive X-ray, transmission electron microscopy, X-ray diffraction, UV−vis diffuse reflectance spectroscopy, photoluminescence, and photoelectrochemical analysis. It was observed that in the presence of the composite of Mg−Al LDH and g-C_3N_4, the photocatalytic decomposition of MB under 150 W mercury lamp illumination increases significantly as opposed to Mg−Al LDH alone, and the Mg−Al LDH@g-C_3N_4 level with Ag_3PO_4 coating causes the complete degradation of MB to occur in less time. The outcomes show that the Mg−Al LDH@g-$C_3N_4$30@$Ag_3PO_4$5 nanocomposite demonstrated the highest photodegradation activity (99%). Scavenger tests showed that the two most effective agents in the photodegradation of MB are holes and hydroxyl radicals, respectively. Finally, a type II heterojunction photocatalytic degradation mechanism for MB by Mg−Al LDH@g-$C_3N_4$30@$Ag_3PO_4$5 was proposed.

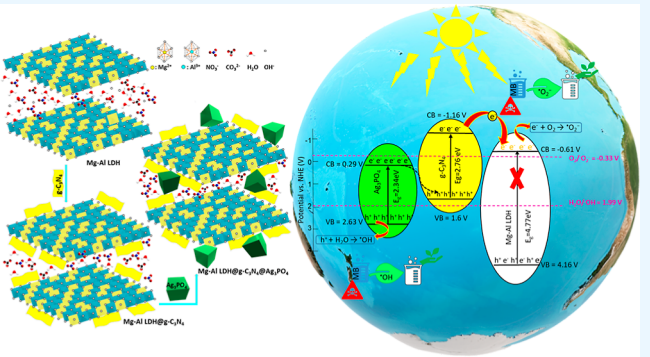

1. INTRODUCTION

The increase in urbanization and the rapid growth of industries, as well as the increase in population and the resulting increase in demand, have caused a severe shortage of clean water resources.[1] Clean water is less readily available due to the contamination of water supplies by industrial dyes, hefty metals, and organic compounds.[2] Therefore, wastewater recycling for reuse is necessary to increase the limited fresh water supply and compensate for potential water resources for a long time.[3] Besides beauty, the dyes make the layers resistant to fading caused by water, light, oxidizing agents, sweat, and microbial attack.[4] This has caused different dyes to be used in various industries such as textile, food, paper, plastic, leather, printing, cosmetics, and medicine for multiple purposes.[5,6] Thus, more than 100,000 commercial paints are produced worldwide, approximately 10^9 kg per year.[7] One of the principal pollutants in wastewater known to cause serious health risks, even in low quantities, is dyes.[8]

Methylene blue (MB) dye is widely used in the textile, paper, wood, and cotton industries, as well as in human and veterinary medicine and research laboratories.[9,10] MB is toxic, carcinogenic, and biostable, and in concentrations higher than the standard, it can cause serious problems for human health and harmful environmental effects.[11] Various techniques have been reported for eliminating contaminants from water, encompassing adsorption,[12] coagulation−flocculation,[13] electrocoagulation,[14] vacuum membrane distillation,[15] nanofiltration,[16] ultrafiltration,[17] and advanced oxidation processes (AOPs).[18−20] AOPs have advantages such as fast reaction speed, decomposition of target compounds into harmless minerals such as CO_2 and H_2O, and providing different routes for generating $OH^•$, $O_2^{•−}$, and other reactive species, which lead to better adaptation to specific treatment needs.[21,22] An example of AOPs is heterogeneous photocatalysis, which has advantages such as low cost, high efficiency, and nontoxicity. With these properties, photocatalysts have the potential to be widely used to remove organic dyes and pesticides.[23,24]

In the past decade, photocatalytic applications based on layered double hydroxides (LDHs) for environmentally

Received: October 4, 2023
Revised: December 22, 2023
Accepted: January 5, 2024
Published: January 22, 2024

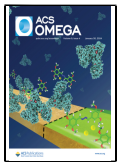

https://doi.org/10.1021/acsomega.3c07326
ACS Omega 2024, 9, 4581−4593

Scheme 1. Preparation Steps of Samples[a]

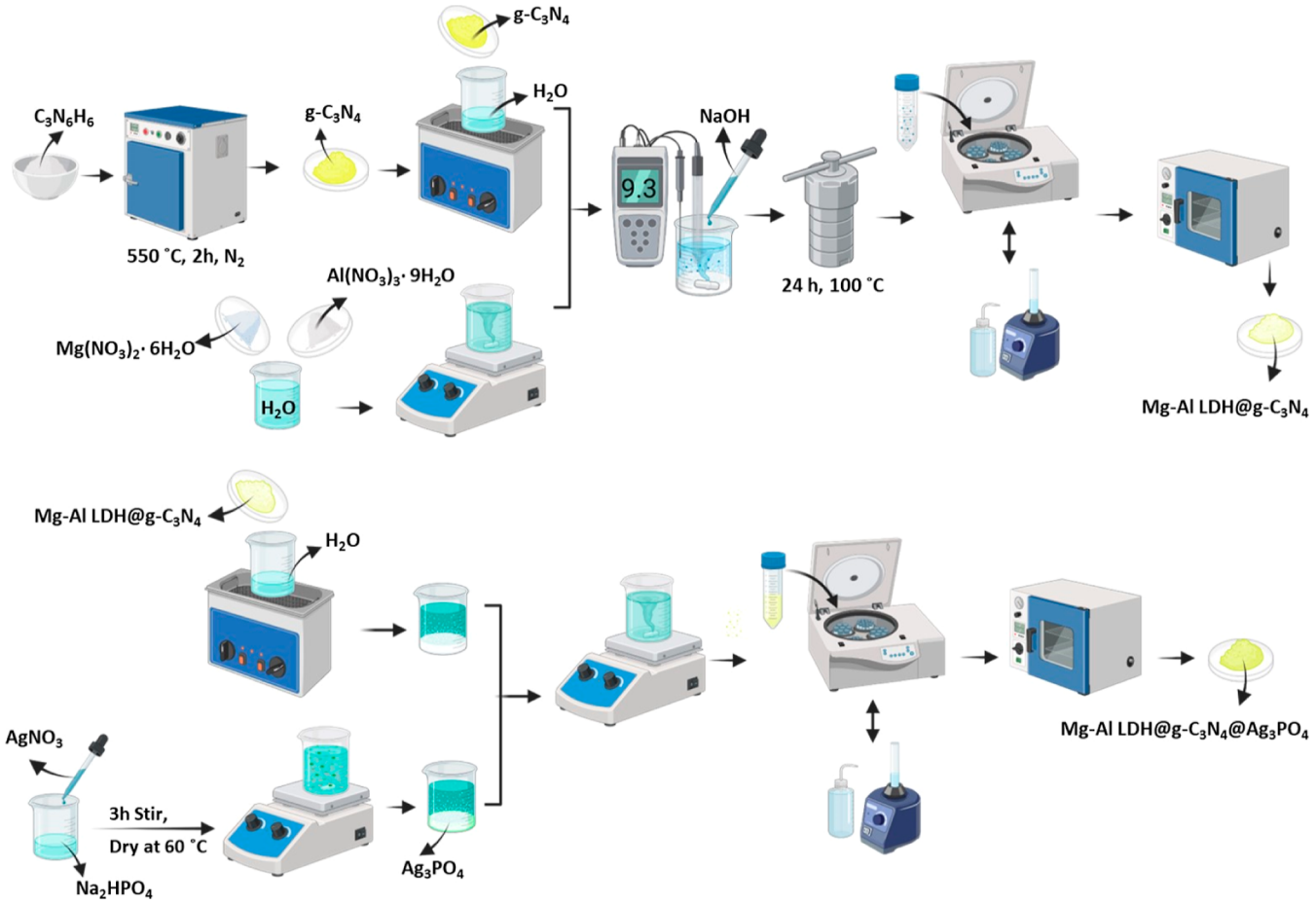

[a]Created with http://BioRender.com.

friendly purposes such as photocatalytic water splitting as a green technology leading to hydrogen (H_2) production, CO_2 reduction, and degradation of harmful substances and toxic organic pollutants as harmless and less toxic has been the focus of researchers. For instance, 2D-C_3N_4/NiFe-LDH has been synthesized and utilized in the H_2 evolution.[25] The CO_2 reduction process has been investigated using a $CsPbBr_3$/CoAl-LDH composite.[26] Additionally, NiAl-LDH/$(BiO)_2CO_3$ has been employed for the photocatalytic degradation of antibiotics,[27] while Al−Li/Th-LDH@CNT has been utilized in the photodegradation of malachite green dye.[28] Furthermore, the decomposition of Congo red and tetracycline has been studied using CoAl-LDH/g-C_3N_4/RGO.[29]

LDHs are cationic layers with the structural formula $[M_{1-x}^{2+}M_x^{3+}\ (OH)_2]^{x+}\ (A^{n-})_{x/n}{\cdot}mH_2O$, where A^{n-} refers to the interlayer anion. M^{2+} and M^{3+} denote metal ions with +2 and +3 charges, respectively.[30] This singular structure gives LDH attractive structural features, including broad selectivity of different metal cations, M^{2+}/M^{3+} molar ratios, tunable interlayer spaces, excellent ion exchange property, oxo-bridged linkages, and exfoliation from bulk LDH solids to functional ultrathin nanosheets.[31] LDH-based photocatalysts are up-and-coming candidates for photocatalytic processes because of their layered structure, defects, adjustable band gap, durability, cost-effectiveness, substantial specific surface area, simple and environmentally friendly synthesis, and ease of scale-up.[32,33] However, rapid electron−hole recombination and sluggish charge carrier mobility lower their photocatalytic efficiency.[34]

In this respect, one possible solution is to create a heterostructure material by combining LDHs with other semiconductors, such as metal-free polymeric carbon nitride (C_3N_4).[35] Unlike other conductive semiconducting polymers, C_3N_4 is thermally and chemically stable, and its preparation is not complex and expensive. C_3N_4 exists in various allotropes with distinct characteristics; nonetheless, the graphitic phase is considered the most stable regarding environmental factors. Graphitic carbon nitride exhibits a band gap of approximately 2.7 eV, indicating its absorption potential in the blue range of the visible spectrum.[36] However, like pure LDHs, g-C_3N_4 alone, its quick photoexcited electron−hole pair recombination decreases its photocatalytic efficiency. Electrostatic interactions can facilitate the assembly of the g-C_3N_4 and LDH layers because LDH and carbon nitride have positive and negative surface charges, respectively.[37,38] Our previous studies demonstrated that the synergist of Ni−Al LDH and g-C_3N_4 limits the recombining of holes and electrons.[39] Although the coupling of LDH and g-C_3N_4 can promote separating holes and electrons, in order to achieve higher photocatalytic efficiency, more and faster transfer of charge carriers is required in some LDH@g-C_3N_4 photocatalysts to participate in electron transfer reactions.[11] Thus, the design of LDH@g-C_3N_4@X ternary photoactive catalysts is regarded. X can be different semiconductors and noble metals. This approach will

https://doi.org/10.1021/acsomega.3c07326
ACS Omega 2024, 9, 4581−4593

facilitate the transfer of current carriers between the junction of g-C_3N_4 and LDH, enhancing the ability to harvest visible light.[40]

Recently, Ag-based compounds such as Ag/ZnO and Ag@AgX (X = I, Br, and Cl) have captured the interest of researchers as promising photocatalysts.[41−43] Silver phosphate, Ag_3PO_4, has been reported as an efficient photocatalyst due to its high quantum yield and visible light response.[44] Compared to other visible light photocatalysts, the reaction rates shown for the photodegradation of organic pollutants are significantly higher. Such remarkable activity is due to the 2.34 eV band gap, enabling the efficient absorption of visible light. Two problems are noticeable in using Ag_3PO_4 as a photocatalyst: (1) poor stability (photocorrosion phenomenon) and formation of metallic silver, and (2) fast rate of recombination of charge carriers produced by light. One approach to solve these problems is to combine Ag_3PO_4 with other semiconductor materials and make heterogeneous composites.[45]

Focusing on the above explanations in mind, to obtain a nanocomposite with significant photocatalytic properties for the degradation of dyes, a ternary nanocomposite between Mg−Al LDH, g-C_3N_4, and Ag_3PO_4 was designed and synthesized. The synthesized compound was named Mg−Al LDH@g-C_3N_4@Ag_3PO_4. According to the latest knowledge, this nanocomposite has been reported for the first time. Achieving 100% degradation of MB dye after 45 min of visible light irradiation is significantly better than previous literature reports.

2. EXPERIMENTAL PROCEDURES

2.1. Preparation of the Mg−Al LDH@g-C_3N_4@Ag_3PO_4 Nanocomposites. 500 mg of Mg−Al LDH@g-$C_3N_4$30 and the appropriate amount of Ag_3PO_4 (5 and 10%) were dispersed separately in 50 mL of deionized (DI) water with 30 min of sonication. Then, both suspension solutions were mixed, and after continuous stirring for 60 min, the precipitate was rinsed with ethanol; to remove any impurities, followed by drying at a 60 °C temperature. In this way, ternary nanocomposites with different Ag_3PO_4 percentages were prepared, and these nanocomposites were determined as Mg−Al LDH@g-$C_3N_4$30@Ag_3PO_4Y (Y = 5 and 10 wt %). The preparation steps of all of the samples are schematically and briefly shown in Scheme 1 and Figure S1.

2.2. Photocatalysis. The effectiveness of the manufactured photocatalysts in the decomposition of MB in aqueous solutions was examined when irradiated with visible light and in the absence of light. For this aim, the suspension was prepared by spreading 50 mg of photocatalyst powder in 0.04 L of MB solution (10 mg L^{-1}) using an ultrasonic bath (200 W). Then, the mixture was magnetically agitated in the absence of light for 15 min to provide the absorption and desorption balance of dye molecules on the photocatalyst surface. After that, the photodegradation test was performed for 45 min under visible light irradiation. A mercury light source (150 W) possessing a 420 nm filter cutoff was employed to provide visible light. To quantify the concentration of MB, samples were taken from the reaction vessel every 15 min, and the catalyst particles were separated by centrifugation (6000 rpm, 5 min). Then, the UV−visible spectra of the solutions were logged by using a UV−visible spectrometer between the wavelengths of 200 and 800 nm. The MB degradation percentage was determined using eq 1, where A_0 and C_0 refer to the initial absorption and initial concentration of MB solution, and A_t and C_t correspond to the absorption and concentration of MB at a specific time (t), respectively,

$$D = \left[1 - \frac{A_t}{A_0}\right] \times 100 = \left[1 - \frac{C_t}{C_0}\right] \times 100 \quad (1)$$

2.3. Photoelectrochemical Measurements. For the measurement of photoelectrochemical properties, a three-electrode quartz cell with a platinum counter electrode (20 mm × 10 mm) and an Ag/AgCl reference electrode were employed in the experiment. To prepare the working electrodes, a uniform ink mixture was made by dispersing 5 mg of the material that had been prepared earlier in 80 μL of ethanol, 300 μL of DI water, and 20 μL of Nafion (5 wt % in ethanol) using an ultrasonic bath. 60 μL of the ink was then drop-cast on top of 1 cm^2 FTO glass, which was fluorine-doped tin oxide glass, undergoing a cleaning process by being washed with ethanol for 30 min using an ultrasonic bath. After cleaning, it was left to dry naturally at room temperature.

The irradiation source for the experiments was a 300 W xenon lamp system, which was furnished with a cutoff filter at 420 nm and applied. The photoelectrode was positioned at a distance of around 3.5 cm from the lamp, and at this distance, the light intensity was 100 m W/cm^2, as measured by a lux meter. Measurements using electrochemical impedance spectroscopy (EIS) were performed in a 0.5 M KCl aqueous electrolyte solution at the open circuit potential, which contained a 0.01 M one-to-one ratio of $K_3[Fe(CN)_6]$/$K_4[Fe(CN)_6]$. Measurements of cyclic voltammograms were conducted in the same electrolyte used for the EIS measurements. Linear sweep voltammetry (LSV) was employed to acquire cathodic polarization curves in an aqueous solution of 0.1 M Na_2SO_4. Photocurrent densities were obtained by the chronoamperometry technique in an aqueous solution of 0.2 M Na_2SO_4, by turning on and off the visible light irradiation every 20 s.

3. RESULTS AND DISCUSSION

3.1. Study of the Synthesized Substances. The Fourier-transform infrared spectroscopy (FT-IR) spectrum of the samples after preparation is shown in Figure 1. As stated in Figure 1, Mg−Al LDH shows two broad bands at around 3460 and 1636 cm^{-1}, which correspond to both symmetric and asymmetric stretching modes of hydroxyl groups, along with water molecule bending modes residing in the surface and the interlayer gallery of LDH nanoplates, respectively. Furthermore, the peak of nitrate and carbonate ion vibrations in the area between layers of Mg−Al LDH appeared in 1366 cm^{-1}. The bands observed at less than 800 cm^{-1} are related to metal−OH (and O) modes.[46,47] According to Figure 1, pure g-C_3N_4 shows a 3200 cm^{-1} broad peak, which correlates with the N−H stretching mode. The bands from 1200 to 1700 cm^{-1} are stretch modes for C−N and C═N, while heptazine ring bending vibrations are responsible for the band at 809 cm^{-1}. In the spectrum of the Mg−Al LDH@g-C_3N_4-X nanocomposites, the vibrational bands of g-C_3N_4 and Mg−Al LDH are discernible. The FT-IR band intensity of binary nanocomposites is increasing with an upward trend in the g-C_3N_4 weight percentage in nanocomposites. Ag_3PO_4 demonstrates that two peaks at 1000 and 564 cm^{-1} are caused by stretching vibration in P−O. According to Figure 1, the presence of characteristic peaks of Mg−Al LDH, pure g-C_3N_4, and Ag_3PO_4

https://doi.org/10.1021/acsomega.3c07326
ACS Omega 2024, 9, 4581−4593

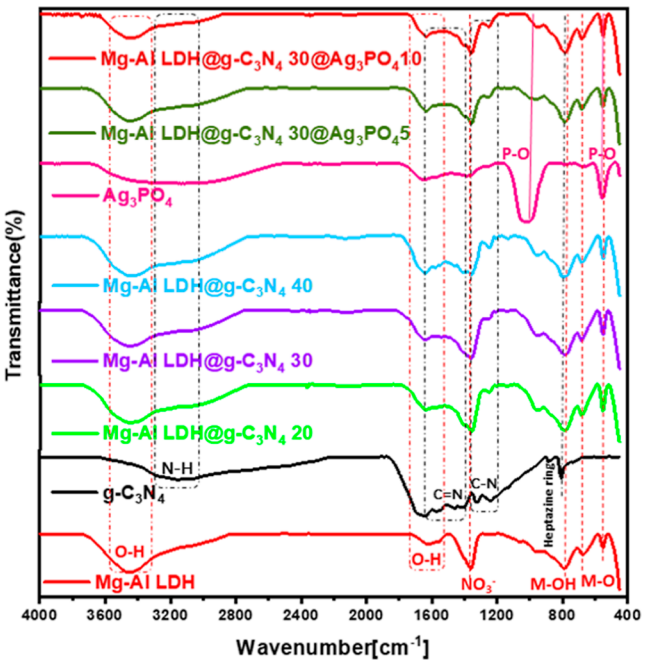

Figure 1. FT-IR spectra of the synthesized samples.

can be an apparent confirmation of the correct preparation of the Mg−Al LDH@g-$C_3N_4$30@Ag_3PO_4-*Y* nanocomposites.[48]

Figure 2 shows the field emission scanning electron microscopy (FE-SEM) images of the produced materials. According to Figure 2a,b, g-C_3N_4 and Mg−Al LDH show an agglomerated and hexagonal-like morphology, respectively, as depicted in Figure 2c, and g-C_3N_4 particles spread on LDH's surface and cover their surface. LDH's hexagonal plates prevent the agglomeration of the g-C_3N_4 particles. In Figure 2d, both spherical and cubic morphologies can be seen in the Ag_3PO_4 particles. Figure 2e illustrates the morphology of Mg−Al LDH@g-$C_3N_4$30@$Ag_3PO_4$5. Due to the minimal amount of Ag_3PO_4 in the nanocomposite, the presence of its particles is not significant. Moreover, transmission electron microscopy (TEM) analysis was performed to determine the presence of three components in the heterostructure. As shown in Figure 2f, the three components overlap well, which is good evidence for the correct synthesis of the heterostructure. The particle size distribution of Mg−Al LDH is somewhat uniform, as confirmed by SEM (Figure S2a) and TEM (Figure S2b−d) images. Conversely, measurements of silver phosphate particles in SEM images (Figure S2e−h) show a broad size distribution, with particles ranging from approximately 100 to 400 nm. To confirm the correct synthesis of the samples, energy-dispersive X-ray (EDX) analysis (Figure S3a−e) and elemental mapping (Figure S3f−j) of the synthesized samples were checked. Figure S3 confirms the presence of the expected elements in the composition of each sample and the proper distribution of the elements.

The X-ray diffraction (XRD) pattern was utilized to analyze the crystalline form of the synthesized materials. According to Figure 3, the pattern for pure Mg−Al LDH shows some distinct diffraction peaks at 11.42, 23.22, 34.27, 39.97, 47.42, 60.82, and 62.27°, which are indexed to (003), (006), (012), (015), (018), (110), and (113) planes, respectively (JCPDS 15-0087).[49] A distinct diffraction peak in the diffraction pattern of pure g-C_3N_4 sample at approximately 27.42° corresponds to the (002) planes of g-C_3N_4 (JCPDS 87-1526).[50] The LDH sample is exceptionally pure and has no impressive peaks. The XRD pattern of Mg−Al LDH@g-$C_3N_4$30 comprises Mg−Al LDH and g-C_3N_4 diffraction peaks. As depicted in Figure 3, the pattern for pure Ag_3PO_4 shows some distinct diffraction peaks at 20.87, 29.72, 33.32, 37.07,

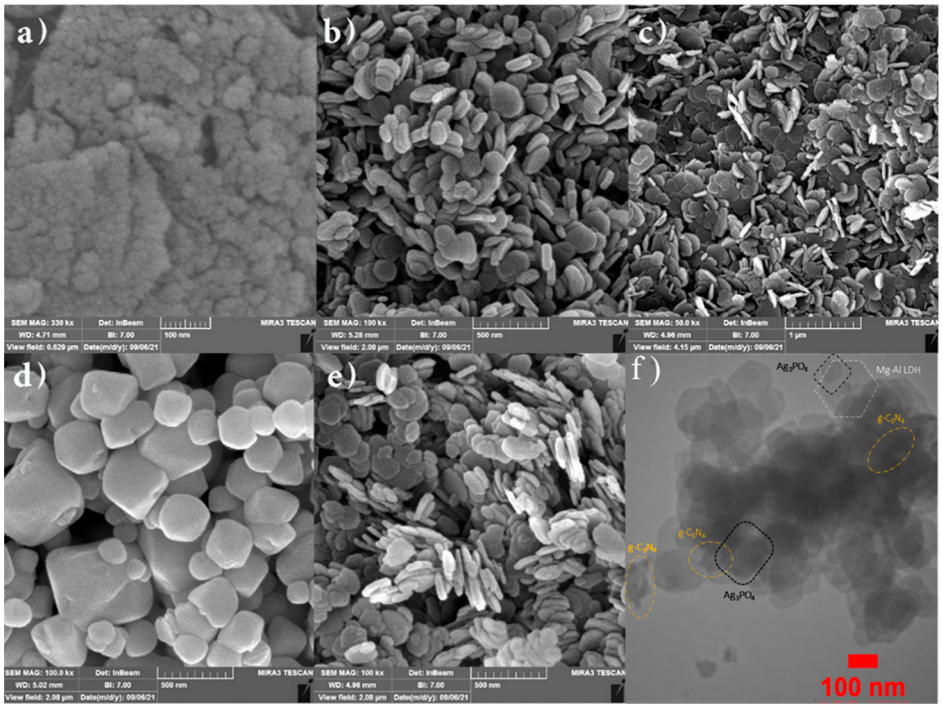

Figure 2. FE-SEM images of the pristine g-C_3N_4 (a), pristine Mg−Al LDH (b), Mg−Al LDH@g-$C_3N_4$30 (c), pure Ag_3PO_4 (d), Mg−Al LDH@g-$C_3N_4$30@$Ag_3PO_4$5 (e), and TEM image of Mg−Al LDH@g-$C_3N_4$30@$Ag_3PO_4$5 (f).

https://doi.org/10.1021/acsomega.3c07326
ACS Omega 2024, 9, 4581−4593

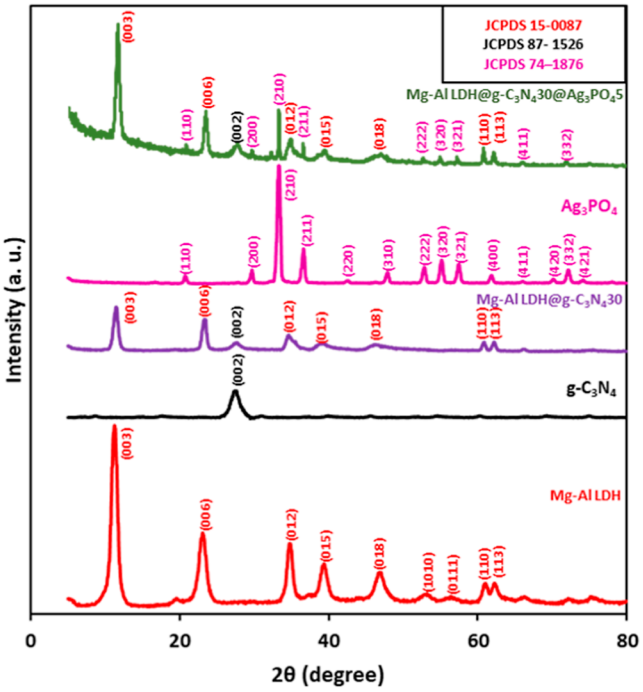

Figure 3. XRD patterns of the synthesized samples.

42.47, 47.82, 52.87, 55.17, 57.37, 61.72, 70.47, 72.07, and 74.72°, which correspond, respectively, to the (110), (200), (210), (211), (220), (310), (222), (320), (321), (400), (420), (421), and (332) planes (JCPDS 74-1876).[51] As seen in Figure 3, all three XRDs of primary constituents are present in the XRD pattern of Mg−Al LDH@g-$C_3N_4$30@$Ag_3PO_4$5, and it shows that the desired nanostructure is well synthesized.

The light absorption characteristics of semiconductor materials have a significant impact on their photocatalytic behavior. Also, the photo response range is a determining factor in the photocatalyst's photodegradation efficiency. In this regard, the optical characteristics and energy band structures of the samples were studied using UV−vis diffuse reflectance spectroscopy (DRS). As stated in Figure 4f, Mg−Al LDH was absorbed in the UV region only and exhibited a steep edge at about 260 nm. Charge transfer from the ligand to the metal causes a significant absorption band below 300 nm.[52] This was expected, as this sample contains M^{2+} cations with d^0 electron configurations; hence, d−d transitions at visible wavelengths were impossible.[53] As shown in Figure 4f, g-C_3N_4 and Ag_3PO_4 display a broad absorption in the spectral range visible with absorption edges located at 449 and 530 nm, respectively. The g-C_3N_4 absorption band edge is assigned to the n* transitions caused by the nitrogen atoms in the triazine and heptazine rings, which possess lone pairs of electrons.[54] Compared to LDH, the Mg−Al LDH@g-$C_3N_4$30 double

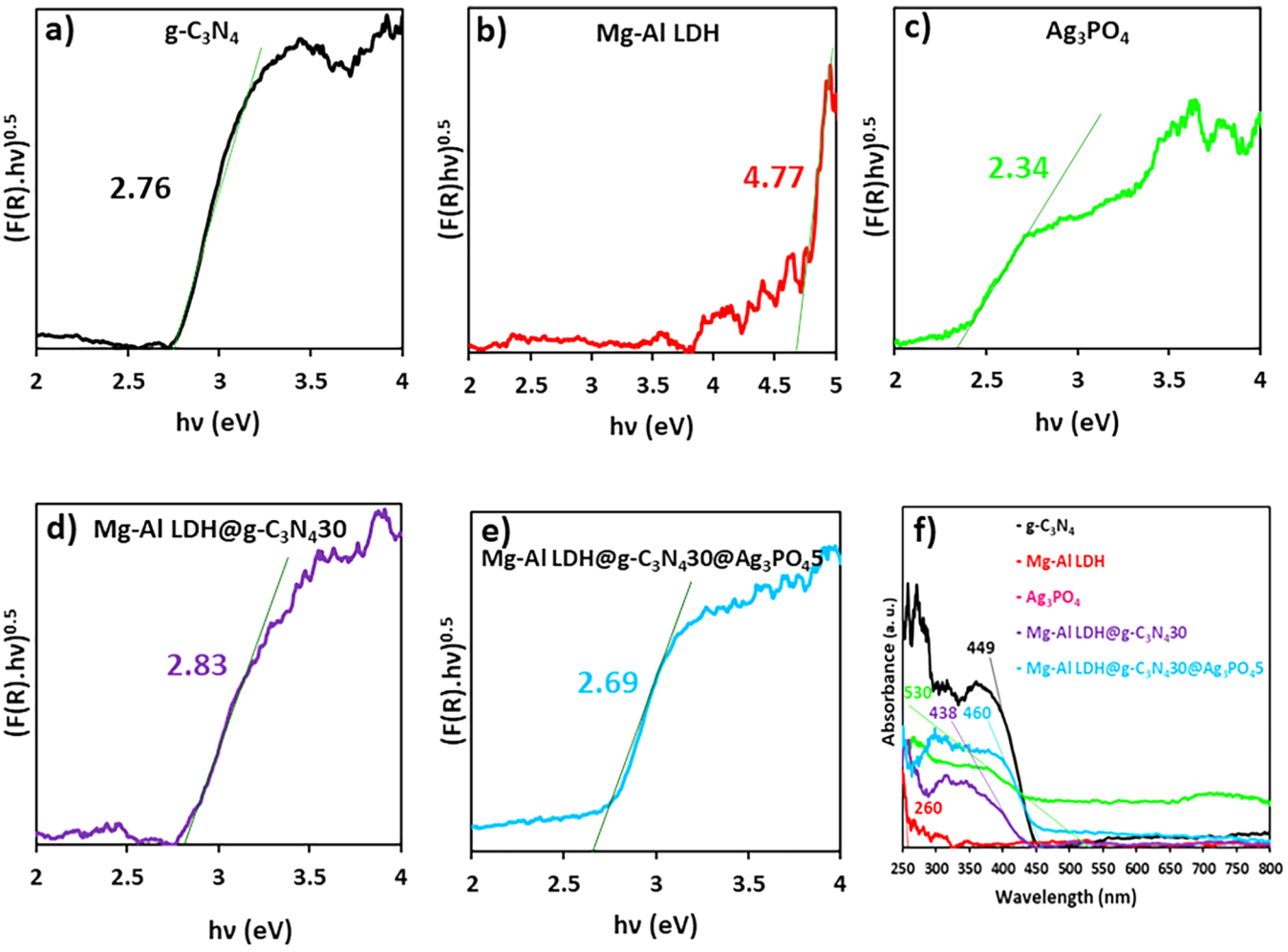

Figure 4. Tauc plots (a−e) and UV−vis DRS (f) of synthesized samples.

https://doi.org/10.1021/acsomega.3c07326
ACS Omega 2024, 9, 4581−4593

composite exhibits a significant shift of the absorption edge toward longer wavelengths because the absorption band covers a more fantastic visible range because of the quantum confinement phenomenon of g-C_3N_4 on Mg−Al LDH and indicates the strong coordination between two components.[40] Upon the loading of Ag_3PO_4, the Mg−Al LDH@g-$C_3N_4$30@$Ag_3PO_4$5 composite possesses improved absorption in the visible spectrum as compared to the other three samples (Mg−Al LDH, g-C_3N_4, and Mg−Al LDH@g-$C_3N_4$30). At present, to estimate the energy of band gap of the samples with DRS results, the functions of Kubelka−Munk (F(R)) and Tauc's equation were used.[55] Estimated band gap energies for pure g-C_3N_4, Mg−Al LDH, Ag_3PO_4, Mg−Al LDH@g-$C_3N_4$30, and Mg−Al LDH@g-$C_3N_4$30@$Ag_3PO_4$5 are 2.76, 4.77, 2.34, 2.83, and 2.69 eV, respectively (Figure 4a−e).

In order to survey and compare the electron−hole recombination and photocatalytic performance of the synthesized samples, the photoluminescence (PL) spectra were noted. Figure 5 shows the PL spectra of the synthesized

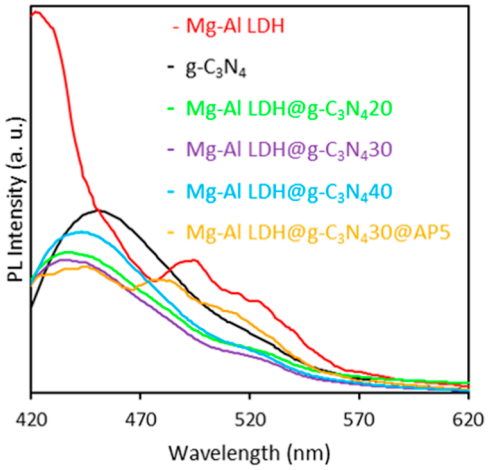

Figure 5. PL spectra of the synthesized samples.

materials. All of the samples were excited at 385 nm and room temperature, and the PL spectra were captured. According to Figure 5, Mg−Al LDH shows a very high-intensity peak. Because of the band−band PL incidence, g-C_3N_4 displays a broad emission peak with a 450 nm central wavelength. The g-C_3N_4 band gap energy is about equivalent to this light energy. As indicated in Figure 5, because of the synergy of LDH and g-C_3N_4, the emission peaks of composites show a blue shift. As a consequence of the suppression of recombination of current carriers, primarily caused by the significant quantum confinement impact of highly distributed g-C_3N_4 on Mg−Al LDH, the PL signal becomes significantly quenched.[40] The maximum quenching is observed for Mg−Al LDH@g-$C_3N_4$30@$Ag_3PO_4$5, indicating that the rate at which electron−hole pairs produced by photons recombine is fiercely repressed. These observations indicate an improvement in photocatalytic performance. Among the binary composites, the Mg−Al LDH@g-$C_3N_4$40 composite shows the highest intensity peak, virtually as intense as g-C_3N_4. A more significant concentration of g-C_3N_4 can protect the active catalytic sites; it is known as the shielding effect.[54]

To study the destiny and transfer of electrons generated by light, a set of photoelectrochemical characterizations were performed on the photocatalysts that intimately correlated to the photoactivity of photocatalysts.[56] As shown in Figure 6, the cyclic voltammetry (CV) curves exhibit both anodic and cathodic peaks for each of the samples, which shows higher current density and faster electron transfer in the Mg−Al LDH@g-$C_3N_4$30@$Ag_3PO_4$5 composite in front of g-C_3N_4, Mg−Al LDH, Mg−Al LDH@g-$C_3N_4$30, and Ag_3PO_4.[57] The redox reaction of Fe(III)/Fe(II) in the electrolyte is responsible for the observed peaks of oxidation and reduction in the cyclic voltammogram. For each sample, the anodic and cathodic peaks in CV demonstrate the current density of the redox reaction of Fe(III)/Fe(II), which indicates faster electron transport between the electrolyte and electrode interface. The preparation method of the electrodes and electrolyte in CV measurements is the same; therefore, the electron transfer rate of the electrode materials is related to the current density of the electrodes.[58,59]

As shown in Nyquist plots of the electrochemical impedance spectra (Figure 6b,c), the Mg−Al LDH@g-$C_3N_4$30@$Ag_3PO_4$5 composite material exhibits a smaller semicircle at higher frequencies in comparison to Mg−Al LDH@g-$C_3N_4$30, Mg−Al LDH, g-C_3N_4, and Ag_3PO_4 indicating a lower resistance for the transfer of charges in the Mg−Al LDH@g-$C_3N_4$30@$Ag_3PO_4$5 composite, which facilitates the transfer of charge carriers.[60] Additionally, Mg−Al LDH@g-$C_3N_4$30 utilized in the synthesis of the primary Mg−Al LDH@g-$C_3N_4$30@$Ag_3PO_4$5 composite shows a smaller semicircle as compared to other mass combinations of Mg−Al LDH@g-C_3N_4X (X = 20 and 40). The EIS Nyquist plots (Figure 6d,e) obtained before illumination exhibit a larger semicircle at higher frequencies compared to the EIS Nyquist plots obtained under illumination (Figure 6b,c), indicating a higher charge-transfer resistance. Nyquist plots (Figure 6f) of Mg−Al LDH@g-$C_3N_4$30@$Ag_3PO_4$5 obtained before and after illumination are almost the same and show no difference in the amount of charge-transfer resistance.

The transient photocurrent responses of Mg−Al LDH, g-C_3N_4, Mg−Al LDH@g-$C_3N_4$30, Ag_3PO_4, and the Mg−Al LDH@g-$C_3N_4$30@$Ag_3PO_4$5 composite measured under in-off intermittent light irradiation are shown in Figure 6g. The high photocurrent density of the Mg−Al LDH@g-$C_3N_4$30@$Ag_3PO_4$5 composite is compared with the low photocurrent density of Mg−Al LDH, Mg−Al LDH@g-$C_3N_4$30, and Ag_3PO_4, implying a longer lifetime for the photogenerated charge carriers.[61] The polarization curves obtained through LSV in Figure 6h revealed an increase in the photocurrent density with an applied negative potential. The composite material exhibited a higher current density compared to those of g-C_3N_4, Mg−Al LDH, Mg−Al LDH@g-$C_3N_4$30, and Ag_3PO_4. This enhanced current density can be attributed to the composite's effective electron transport mechanism, indicating its enhanced photoactivity.[62] These findings suggest that the composite possesses favorable characteristics, including a large surface area, abundant active sites for redox reactions, and a reduced charge-transfer resistance. As a result, the generation and transportation of charge carriers to the electrolyte under light illumination are facilitated.[63,64] The above observation cooperatively validates that the Mg−Al LDH@g-$C_3N_4$30@$Ag_3PO_4$5 composited from Mg−Al LDH, Mg−Al LDH@g-$C_3N_4$30, and Ag_3PO_4 aids in facilitating the efficacious transferring and separating charge carriers, thus enhancing the efficiency of the photocatalytic activity.

The diagrams in Figure 7a−d depict the Bode phase and Bode magnitude plot, respectively, which displays the change

https://doi.org/10.1021/acsomega.3c07326
ACS Omega 2024, 9, 4581−4593

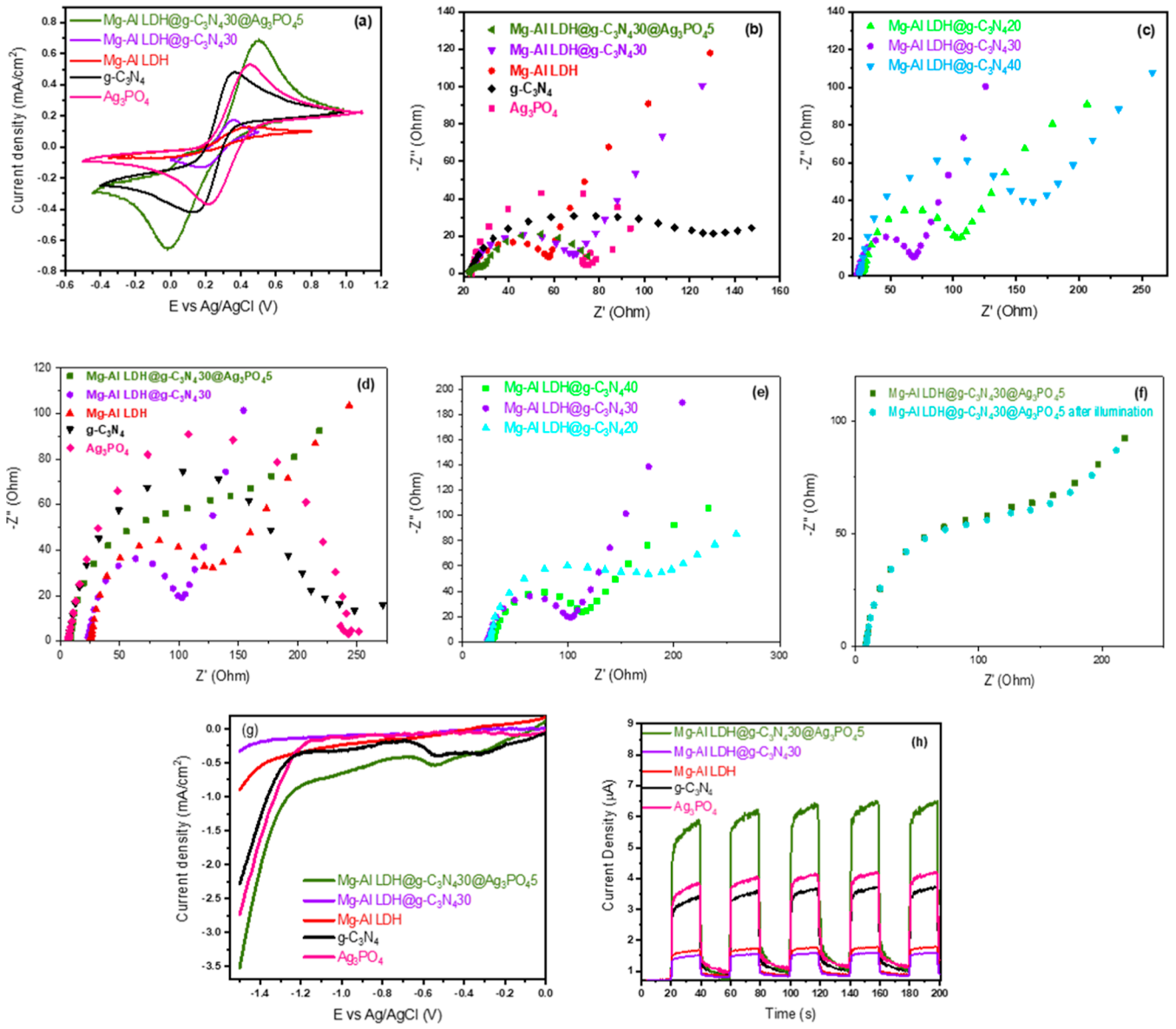

Figure 6. (a) CV curves, (b,c) EIS Nyquist plots, (d,e) EIS Nyquist plots obtained before illumination, with (f) corresponding to the after-illuminated state, (g) LSV transient photocurrent responses of Mg−Al LDH, Mg−Al LDH@g-$C_3N_4$30, g-C_3N_4, Ag_3PO_4, and the Mg−Al LDH@g-$C_3N_4$30@$Ag_3PO_4$5 nanocomposite, (h).

in phase angle for frequency, and the Bode magnitude plot illustrates the changes in impedance magnitude (|Z|) to frequency. The measurements were taken in an aqueous electrolyte with a 1:1 ratio of 0.01 M $K_3[Fe(CN)_6]$ and $K_4[Fe(CN)_6]$ under light and across a frequency span of 1 to 10^5 Hz. The data was obtained from EIS, Figure 6, in the manuscript. Using the *fm* value obtained from the Bode phase plot, which represents the frequency at which the maximum phase angle occurs, the characteristic lifetime of electrons (τ) can be calculated as ($\tau = 1/2\pi fm$).[65] The electron lifetime values for the Mg−Al LDH@g-$C_3N_4$30@$Ag_3PO_4$5, Mg−Al LDH@g-$C_3N_4$30, Mg−Al LDH, g-C_3N_4, and Ag_3PO_4 photoanodes were found to be 58, 0.6, 0.4, 1, and 1 ms, respectively. The three-component nanocomposite exhibited greater electron lifetime (τ) values, which suggests a reduced rate of charge carrier recombination within these materials.[66,67]

3.2. Photocatalysis. The effect of the existence of Mg−Al LDH, g-C_3N_4, Mg−Al LDH@g-C_3N_4X, and the Mg−Al LDH@g-C_3N_4X@Ag_3PO_4Y composite on photocatalytic decomposition of MB under irradiation with visible light was investigated. Figure 8 (and Figure S4) depicts the photocatalytic breakdown of MB after 45 min of exposure to visible light. In order to achieve an equilibrium between the molecules of dye and the photocatalyst, the MB solutions were magnetically agitated for 15 min in the dark before beginning the catalyzed degradation reactions. As shown in Figure 8, the surface adsorption of dye by Mg−Al LDH, g-C_3N_4, Mg−Al LDH@g-$C_3N_4$20, Mg−Al LDH@g-$C_3N_4$30, Mg−Al LDH@g-$C_3N_4$40, Mg−Al LDH@g-$C_3N_4$30@$Ag_3PO_4$5, and Mg−Al LDH@g-$C_3N_4$30@$Ag_3PO_4$10 is recorded as 7, 80, 42, 51, 42, 43, and 33%, respectively. Following 45 min of visible light irradiation, the color removal percentages escalate to 26, 92, 61, 82, 75, 99, and 75%, respectively. These results highlight the distinctive photocatalytic degradation potential exhibited by each sample. The MB removal percentage in the presence of Mg−Al LDH is relatively low. On the other hand, although the

https://doi.org/10.1021/acsomega.3c07326
ACS Omega 2024, 9, 4581−4593

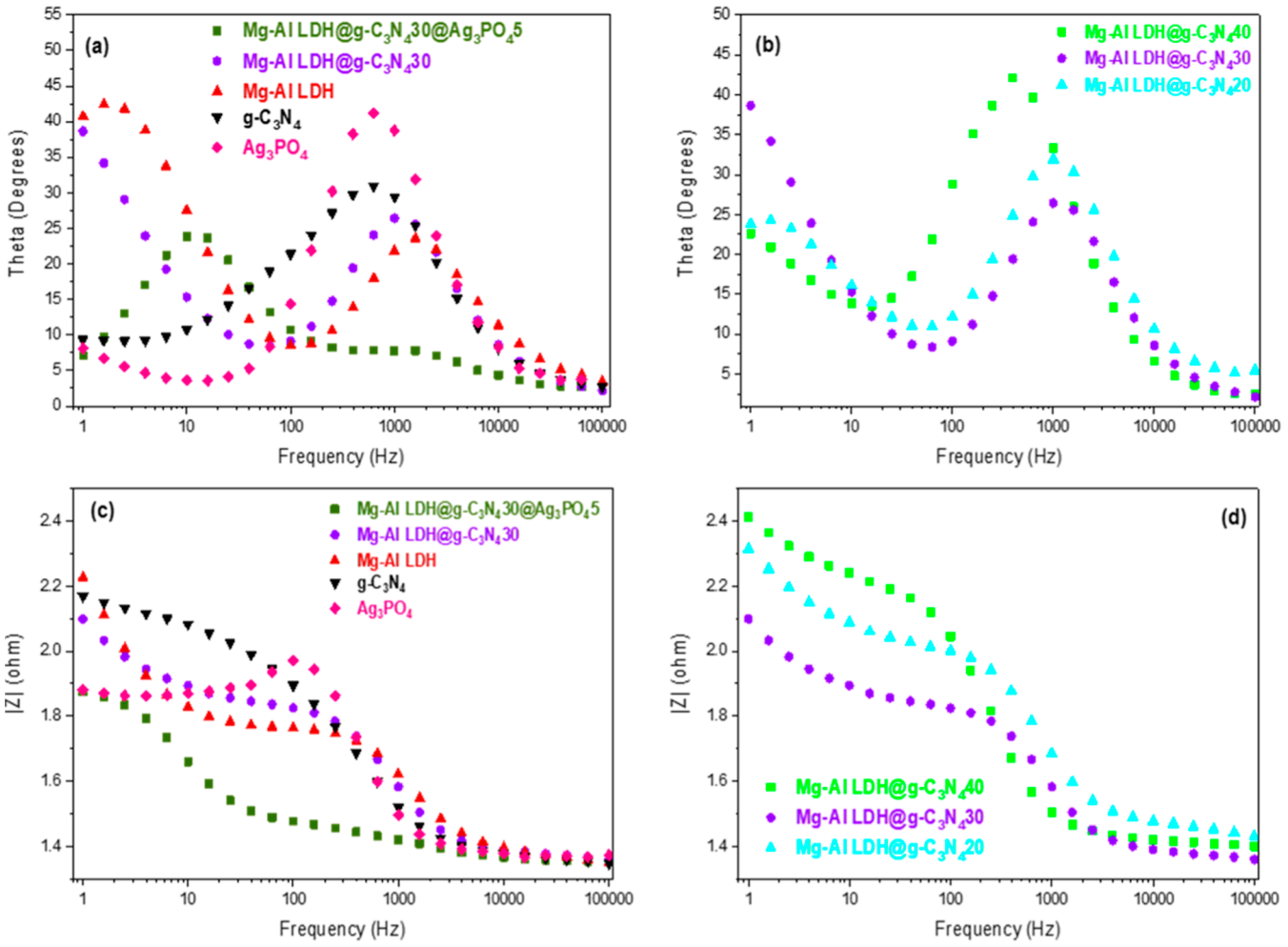

Figure 7. Bode phase (a,b) and Bode magnitude (c,d) plots acquired from EIS measurements for the photoanodes in their as-prepared state.

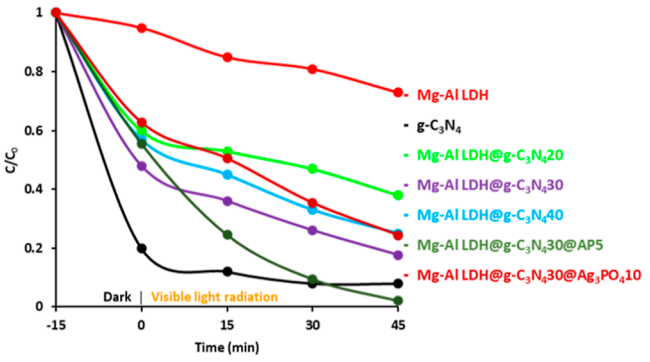

Figure 8. Photocatalytic efficacy of the prepared compounds.

percentage of dye removal is high in the presence of g-C_3N_4, g-C_3N_4 primarily acts as an adsorbent. The high adsorption of MB by g-C_3N_4 depends on the surface area and negative surface charge of g-C_3N_4, leading to the adsorption of cationic pollutant MB through electrostatic interactions. As shown in Figure 8, in the presence of g-C_3N_4, the concentration of MB remains almost constant after the dark period and under light irradiation, and g-C_3N_4 remains in the reaction vessel as a blue sludge due to the absorption of MB at the end of the reaction. This observation emphasizes that in the presence of g-C_3N_4, mainly the adsorption process occurs, and the photocatalytic degradation is negligible; in contrast, Mg−Al LDH@g-C_3N_4X nanocomposites exhibit more photocatalytic activity within the same time. Mg−Al LDH@g-C_3N_4X (X = 20, 30, and 40 wt %) eliminates about 61, 82, and 75% of MB at the maximum point (45 min), respectively. Given this, the increase in the photocatalytic function of composites is in light of the combination of two components. Furthermore, the g-C_3N_4 weight percentage is an essential variable determining the photocatalytic effectiveness of the nanocomposites. Upping the g-C_3N_4 content to 30% from 20% leads to an improvement in the efficiency of MB degradation. However, increasing the concentration of g-C_3N_4 to 40% lacks an effect in enhancing the photocatalytic function. Owing to this, the best g-C_3N_4 content for nanocomposite is 30 wt %. By addition of Ag_3PO_4, the MB degradation efficiency increases. The Mg−Al LDH@g-$C_3N_4$30@$Ag_3PO_4$5 nanocomposite is the optimal photocatalyst, and it can provide 99% MB degradation efficiency under the illumination of visible light in 45 min. The completely clear solution and the absence of MB particles on the catalyst surface after the reaction in the presence of Mg−Al LDH@g-C_3N_4X@$Ag_3PO_4$5 confirm the photocatalytic degradation of MB by Mg−Al LDH@g-C_3N_4X@$Ag_3PO_4$5. The changes in the absorbance of the MB solution after its reaction with prepared compounds under the influence of visible light are illustrated in Figure S5. In addition, in order to research the impact of dye surface absorption and desorption, the absorption of MB by pure Mg−Al LDH, pure g-C_3N_4, and

https://doi.org/10.1021/acsomega.3c07326
ACS Omega 2024, 9, 4581−4593

Mg−Al LDH@g-$C_3N_4$30@$Ag_3PO_4$5 was investigated in the absence of light. The UV−visible absorption spectra of MB dye after 60 min in dark conditions are shown in Figure S6. Based on observations, the surface absorption of MB by Mg−Al LDH@g-$C_3N_4$30@$Ag_3PO_4$5, pure Mg−Al LDH, and pure g-C_3N_4 is about 43, 7, and 88%, respectively. g-C_3N_4 has a high absorption potential for dye removal, while Mg−Al LDH absorbs a low percentage of dye. In the presence of g-C_3N_4, the characteristics of Mg−Al LDH 's absorption are enhanced.

One of the parameters that must be studied in photocatalytic reactions is the amount of photocatalyst used. At the saturation level, the photon absorption coefficient does not increase with an increasing catalyst dosage. The active surface of the reaction decreases due to the covering of active sites by extra photocatalyst particles, ultimately reducing the photocatalytic activity. Thus, the highest effectiveness can be observed with a particular quantity of the photocatalyst. In this study, 10 ppm MB solution was photocatalytically degraded in the presence of 0.3, 0.5, and 0.7 g of Mg−Al LDH@g-$C_3N_4$30@$Ag_3PO_4$5. According to Figure 9 (and Figure S7), the proper amount of

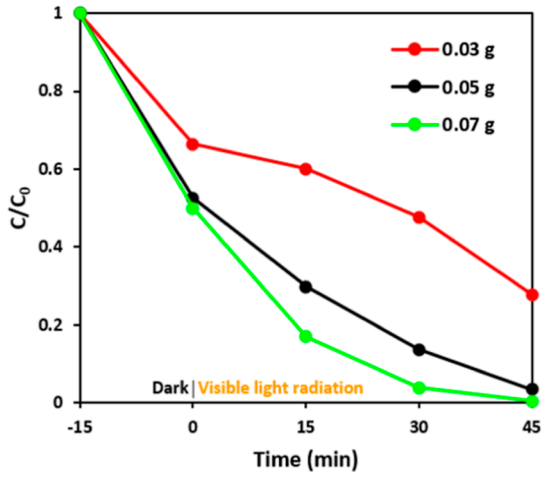

Figure 9. Effects of the amount of Mg−Al LDH@g-$C_3N_4$30@$Ag_3PO_4$5 for MB decomposition.

the photocatalyst for MB removal was determined to be 0.5 g of the nanocomposite. Figure S8 shows the absorption changes in the MB concentration in different dosages of the prepared nanocomposite.

The pH of the reaction medium is another effective parameter in photocatalytic processes. In fact, due to various surface properties, each semiconductor has a different activity at a different pH.[68] Three 40 mL solutions containing ten ppm of MB were prepared for this purpose. The pH of the solutions was set to 3 (acidic), 7 (neutral), and 11 (basic) to determine the optimum pH for MB photocatalytic decomposition. Figure 10 (and Figure S9) illustrates the results. Considering Figure 10, the pH value confirmed that the maximum degradation of MB was 11. The results of the zeta potential test show that at pH = 3, the nanocomposite shows a positive surface charge and a negative 1 at pH = 11 (Figure S10). The positively charged surface of the nanocomposite, along with the presence of positively charged hydronium ions at acidic pH, leads to repulsion among the nanocomposite, MB, and hydronium ions. As a result, this repulsion reduces MB absorption of the photocatalyst. That is why the degradation of MB at pH = 3 is less significant compared to pH = 7 and 11. Figure 10 verifies

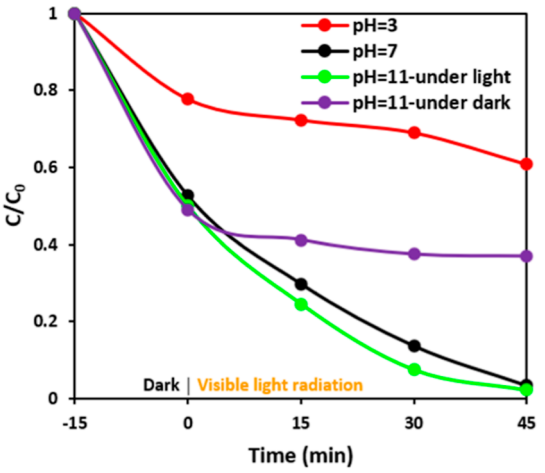

Figure 10. Impact of pH on MB dye degradation by photocatalysis.

this conclusion by describing the least amount of dye decomposition at a pH of 3. Two things stand out in Figure 11. First, MB adsorption on the nanocomposite is lower under

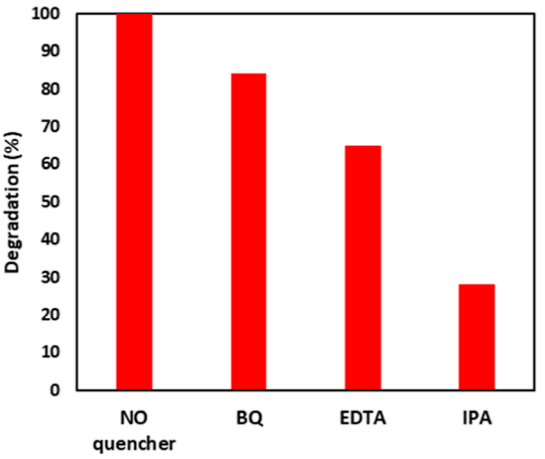

Figure 11. Effects of different scavengers on the decomposition of MB paint by the Mg−Al LDH@g-$C_3N_4$30@$Ag_3PO_4$5 nanocomposite after 45 min of exposure to visible light.

acidic conditions. Since MB, hydronium ions, and the positively charged surface of the nanocomposite repel each other, this prevents MB from sticking to the catalytic surface. Second, because positive charges repel each other in an acidic solution, MB is less likely to adsorb, even under dark conditions. Considering the importance of absorption in pollutant decomposition, MB absorption was investigated in dark conditions at optimal pH and catalyst dosage (pH 11, 0.05 g photocatalyst). In this condition, 62% of dye absorption occurred. The high adsorption of MB is due to its cationic nature and the negative surface charge of the nanocomposite, which promotes cationic MB adsorption on the nanocomposite surface. Figure 10 illustrates how the nanocomposite's surface charges affect dye absorption. The UV−visible absorption spectra of Mg−Al LDH@g-$C_3N_4$30@$Ag_3PO_4$5 nanocomposites for MB decomposition in the presence of light at three different pH values and dark conditions at optimal pH are shown in Figure S11.

Total organic carbon (TOC) estimation was used to determine the mineralization efficiency. The maximum TOC

https://doi.org/10.1021/acsomega.3c07326
ACS Omega 2024, 9, 4581−4593

removal efficiency was 88%, and the MB removal efficiency was 99%. Therefore, the MB dye was mineralized at a high percentage. The outcomes are displayed in Table 1.

Table 1. MB and TOC Removal Efficiency (%) under Light Irradiation

MB			TOC		
initial (mg/L)	final (mg/L)	efficacy of degradation (%)	initial (mg/L)	final (mg/L)	TOC removal efficiency (%)
10	0.1	99	3.51	0.42	88

The stability of the nanocomposite structure after photocatalytic processes was investigated by XRD pattern and FE-SEM images of the Mg−Al LDH@g-$C_3N_4$30@$Ag_3PO_4$5 nanocomposite. The obtained results confirm its structural and morphological stability (Figure S12).

To elucidate the photodegradation mechanism of MB, we identified the key oxidants participating in the process. In this regard, the produced oxidants were trapped and measured using IPA, EDTA-2Na, and BQ, which act as scavengers of hydroxyl radicals, holes, and superoxide radical anions ($O_2^{\bullet-}$), respectively. According to Figure 11, adding IPA significantly lowers the rate of MB photodegradation by the ideal nanocomposite; meanwhile, BQ and EDTA-2Na are more ineffective when added. As a result, all three components are active species in catalytic dye photodegradation. From the electronic point of view, the valence band (VB) electrons travel to the conduction band (CB) when photons with energies equal to or over the band gap are absorbed, and holes are also created in the VB at the exact moment. The results of the scavenger experiments show that the active species, hydroxyl radical, hole, and superoxide ion, were involved in the degradation of MB to the mineralized products. Based on this, and with the help of VB and CB calculations of Mg−Al LDH, g-$C_3N_4$30, and Ag_3PO_4, a possible photocatalytic decomposition mechanism of MB by Mg−Al LDH@g-$C_3N_4$30@$Ag_3PO_4$5 is proposed in Figure 12. Equations 2 and 3 were used to determine the compound's CB and VB potential values, where X is the absolute electronegativity (Mulliken) of material atoms, which can be defined as the geometric mean of their absolute electronegativity. In other words, the arithmetic mean of the initial ionization energy and the atomic electron affinity is defined as X (eq 4). E_e and E_g represent hydrogen-scale free electron energy (~4.50 eV) and band gap energy, respectively,[69]

$$E_{CB} = X - E_e - 0.5E_g \quad (2)$$

$$E_{VB} = E_{CB} + E_g \quad (3)$$

$$X = 0.5(E_{EA} + E_{ion}) \quad (4)$$

As a result of irradiation from a visible light source, electrons are excited on g-C_3N_4 and Ag_3PO_4, and electrons move from the VB of these semiconductor materials to the CB (eq 5). The

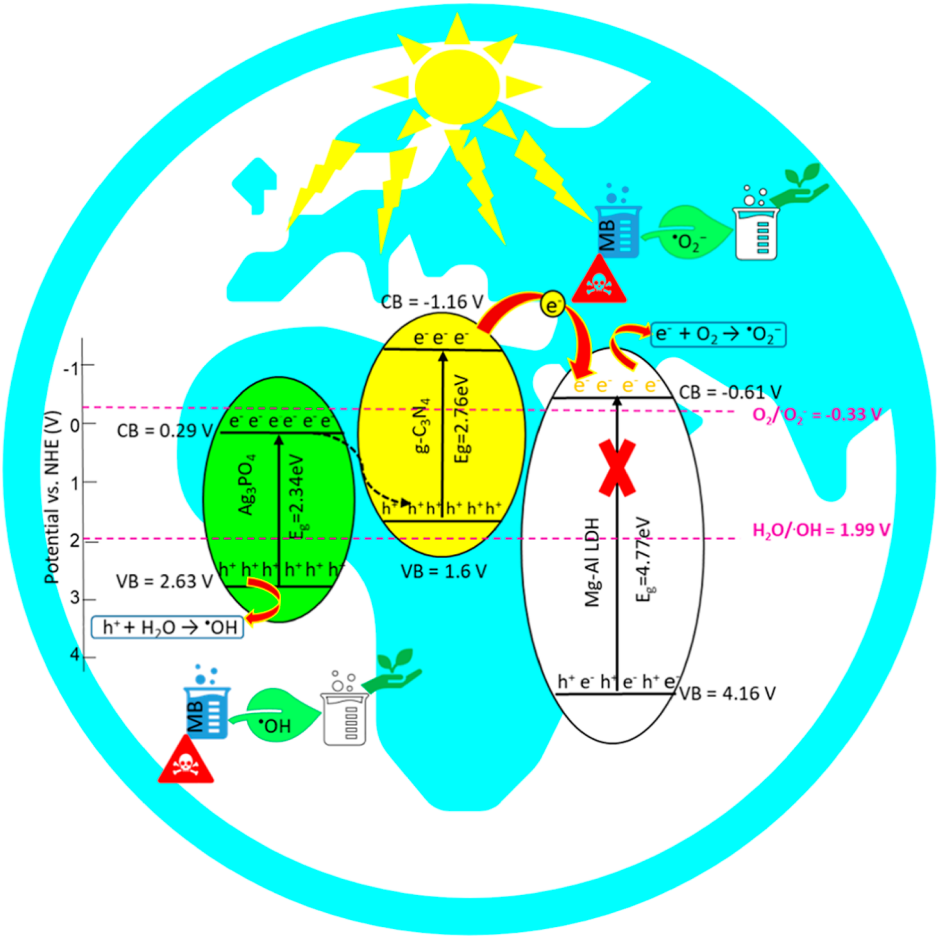

Figure 12. MB photocatalytic decomposition by the Mg−Al LDH@g-$C_3N_4$30@$Ag_3PO_4$5 nanocomposite: a proposed mechanism.

https://doi.org/10.1021/acsomega.3c07326
ACS Omega 2024, 9, 4581−4593

CB level of Ag_3PO_4 is closer to the g-C_3N_4 VB level; hence the electrons stimulated by the light of Ag_3PO_4 would recombine with the holes created by the light of g-C_3N_4 (eq 6). From the combination of VB holes (2.63 V) of Ag_3PO_4 with H_2O, hydroxyl radicals ($OH^\bullet$) are produced ($H_2O/OH^\bullet$ = 1.99 V vs NHE)[70] and would take part in MB oxidation (eqs 10 and 12).

Given that g-C_3N_4's CB position is more negative, electrons migrate from this position to the CB of Mg−Al LDH (eq 8). The CB of Mg−Al LDH (−0.61 V) has a lesser potential than usual for superoxide radicals ($O_2/O_2^{\bullet-}$ = −0.33 V vs NHE).[70] As a result, LDH can produce $O_2^{\bullet-}$ by reducing the adsorbed molecule of oxygen (eq 9). Then, produced $O_2^{\bullet-}$ participates in the degradation reaction of MB (eq 11). Also, these transitions lead to reduced electron−hole pair recombination, which is beneficial for enhancing photocatalytic efficiency.[21] In the end, reactive species are formed to cause the degradation of MB.

The photocatalytic reactions occurring in the Mg−Al LDH@g-$C_3N_4$30@$Ag_3PO_4$5 composite could be summed up by the equations below

$$\text{g} - C_3N_4/Ag_3PO_4 + h\nu \rightarrow \text{g} - C_3N_4(e^- + h^+)/Ag_3PO_4(e^- + h^+) \quad (5)$$

$$\text{g} - C_3N_4(h^+) + Ag_3PO_4(e^-) \rightarrow \text{recombination of } e^- + h^+ \quad (6)$$

$$\text{recombination of } e^-(Ag_3PO_4) + h^+(\text{g-}C_3N_4) \rightarrow \text{g-}C_3N_4(e^-)/Ag_3PO_4(h^+) \quad (7)$$

$$\text{electron migration from CB g-}C_3N_4\text{to CB Mg} - \text{Al LDH} \rightarrow \text{Mg} - \text{Al LDH}(e^-) \quad (8)$$

$$\text{Mg} - \text{Al LDH}(e^-) + O_2 \rightarrow O_2^{\bullet-} \quad (9)$$

$$Ag_3PO_4(h^+) + H_2O \rightarrow OH \quad (10)$$

$$O_2^{\bullet-} + \text{MB} \rightarrow H_2O + CO_2 \quad (11)$$

$$OH^\bullet + \text{MB} \rightarrow H_2O + CO_2 \quad (12)$$

The Mg−Al LDH@g-$C_3N_4$30@$Ag_3PO_4$5 composite shows superior performance in MB dye degradation as evaluated by parameters such as degradation time, light source type and power, and degradation percentage. It outperforms many catalysts designed based on Mg−Al LDH and other compounds. Several reports comparing its performance with other catalysts are listed in Table S1.

4. CONCLUSIONS

In this work, the new nanocomposite of Mg−Al LDH@g-$C_3N_4$30@$Ag_3PO_4$5 was designed and synthesized using a hydrothermal method and showed enhanced photocatalysis in the decomposition of MB dye. The key factor contributing to the enhanced photocatalytic efficiency is the intimate interface among Mg−Al LDH, g-C_3N_4, and Ag_3PO_4. This unique heterojunction architecture facilitates rapid charge-transfer processes, improving the photocatalytic efficiency. Additionally, the reduced arc of the Nyquist plot indicates efficient charge separation and reduced charge recombination, contributing to the increased photocatalytic efficiency of the nanocomposite. Notably, Mg−Al LDH@g-$C_3N_4$30@$Ag_3PO_4$5 exhibited greater photocatalytic efficiency in the degradation of MB compared with Mg−Al LDH, g-C_3N_4, Ag_3PO_4, and Mg−Al LDH@g-$C_3N_4$30. These results demonstrate the potential of LDH-based photocatalysts for achieving maximum photon absorption and effective environmental remediation.

■ ASSOCIATED CONTENT

Supporting Information

The Supporting Information is available free of charge at https://pubs.acs.org/doi/10.1021/acsomega.3c07326.

Materials and methods, material synthesis method, EDX spectra, dye degradation's UV−vis absorption spectrum, photodegradation spectrum in percent, zeta potential diagrams, and FE-SEM images and XRD pattern after photocatalysis (PDF)

■ AUTHOR INFORMATION

Corresponding Author

Mojtaba Bagherzadeh − *Chemistry Department, Sharif University of Technology, Tehran 19166, Iran;* orcid.org/0000-0003-3009-3693; Email: bagherzadeh@sharif.edu

Authors

Ghazal Salehi − *Chemistry Department, Sharif University of Technology, Tehran 19166, Iran*

Reza Abazari − *Chemistry Department, Faculty of Science, University of Maragheh, Maragheh 83111, Iran;* orcid.org/0000-0002-3725-2557

Mojtaba Hajilo − *Chemistry Department, Sharif University of Technology, Tehran 19166, Iran*

Davood Taherinia − *Chemistry Department, Sharif University of Technology, Tehran 19166, Iran;* orcid.org/0000-0002-3097-766X

Complete contact information is available at: https://pubs.acs.org/10.1021/acsomega.3c07326

Notes

The authors declare no competing financial interest.

■ ACKNOWLEDGMENTS

The Research Council of Iran's Sharif University of Technology provided funding for this work. The authors appreciate the financial assistance.

■ REFERENCES

(1) Dong, S.; Feng, J.; Fan, M.; Pi, Y.; Hu, L.; Han, X.; Liu, M.; Sun, J.; Sun, J. Recent developments in heterogeneous photocatalytic water treatment using visible light-responsive photocatalysts: a review. *RSC Adv.* **2015**, *5* (19), 14610−14630.

(2) Deng, H.; Yin, J.; Ma, J.; Zhou, J.; Zhang, L.; Gao, L.; Jiao, T. Exploring the enhanced catalytic performance on nitro dyes via a novel template of flake-network Ni-Ti LDH/GO in-situ deposited with Ag_3PO_4 NPs. *Appl. Surf. Sci.* **2021**, *543*, 148821.

(3) Qu, J.; Fan, M. The current state of water quality and technology development for water pollution control in China. *Crit. Rev. Environ. Sci. Technol.* **2010**, *40* (6), 519−560.

(4) Khan, I.; Khan, I.; Usman, M.; Imran, M.; Saeed, K. Nanoclay-mediated photocatalytic activity enhancement of copper oxide nanoparticles for enhanced methyl orange photodegradation. *J. Mater. Sci.: Mater. Electron.* **2020**, *31* (11), 8971−8985.

(5) Bhat, A. P.; Gogate, P. R. Degradation of nitrogen-containing hazardous compounds using advanced oxidation processes: a review on aliphatic and aromatic amines, dyes, and pesticides. *J. Hazard. Mater.* **2021**, *403*, 123657.

https://doi.org/10.1021/acsomega.3c07326
ACS Omega 2024, 9, 4581−4593

(6) Javaid, R.; Qazi, U. Y. Catalytic oxidation process for the degradation of synthetic dyes: an overview. *Int. J. Environ. Res. Public Health* **2019**, *16* (11), 2066.
(7) Bouras, H. D.; Isik, Z.; Arikan, E. B.; Yeddou, A. R.; Bouras, N.; Chergui, A.; Favier, L.; Amrane, A.; Dizge, N. Biosorption characteristics of methylene blue dye by two fungal biomasses. *Int. J. Environ. Stud.* **2021**, *78* (3), 365−381.
(8) Kaveh, R.; Bagherzadeh, M. Simultaneous removal of mercury ions and cationic and anionic dyes from aqueous solution using epichlorohydrin cross-linked chitosan@ magnetic Fe_3O_4/activated carbon nanocomposite as an adsorbent. *Diam. Relat. Mater.* **2022**, *124*, 108923.
(9) Houas, A.; Lachheb, H.; Ksibi, M.; Elaloui, E.; Guillard, C.; Herrmann, J.-M. Photocatalytic degradation pathway of methylene blue in water. *Appl. Catal., B* **2001**, *31* (2), 145−157.
(10) Hou, C.; Hu, B.; Zhu, J. Photocatalytic degradation of methylene blue over TiO_2 pretreated with varying concentrations of NaOH. *Catalysts* **2018**, *8* (12), 575.
(11) Zhang, P.; Xiang, M.; Liu, H.; Yang, C.; Deng, S. Novel two-dimensional magnetic titanium carbide for methylene blue removal over a wide pH range: insight into removal performance and mechanism. *ACS Appl. Mater. Interfaces* **2019**, *11* (27), 24027−24036.
(12) Abazari, R.; Salehi, G.; Mahjoub, A. R. Ultrasound-assisted preparation of a nanostructured zinc (II) amine pillar metal-organic framework as a potential sorbent for 2, 4-dichlorophenol adsorption from aqueous solution. *Ultrason. Sonochem.* **2018**, *46*, 59−67.
(13) Lau, Y.-Y.; Wong, Y.-S.; Teng, T.-T.; Morad, N.; Rafatullah, M.; Ong, S.-A. Degradation of cationic and anionic dyes in coagulation-flocculation process using bi-functionalized silica hybrid with aluminum-ferric as auxiliary agent. *RSC Adv.* **2015**, *5* (43), 34206−34215.
(14) Golder, A.; Hridaya, N.; Samanta, A.; Ray, S. Electro-coagulation of methylene blue and eosin yellowish using mild steel electrodes. *J. Hazard. Mater.* **2005**, *127* (1−3), 134−140.
(15) Mukherjee, A.; Satish, A.; Mullick, A.; Rapolu, J.; Moulik, S.; Roy, A.; Ghosh, A. K. Paradigm Shift toward Developing a Zero Liquid Discharge Strategy for Dye-Contaminated Water Streams: A Green and Sustainable Approach Using Hydrodynamic Cavitation and Vacuum Membrane Distillation. *ACS Sustainable Chem. Eng.* **2021**, *9* (19), 6707−6719.
(16) Qu, H.; Xiao, X.; Han, Z.; Hu, M.; Shen, S.; Yang, L.; Jia, F.; Wang, T.; Ye, Z.; Sun, W.; et al. Graphene Oxide Nanofiltration Membrane Based on Three-Dimensional Size-Controllable Metal-Organic Frameworks for Water Treatment. *ACS Appl. Nano Mater.* **2022**, *5* (4), 5196−5207.
(17) Kim, S.; Yu, M.; Yoon, Y. Fouling and retention mechanisms of selected cationic and anionic dyes in a Ti_3C_2T x MXene-ultrafiltration hybrid system. *ACS Appl. Mater. Interfaces* **2020**, *12* (14), 16557−16565.
(18) Mokhtarifar, M.; Kaveh, R.; Bagherzadeh, M.; Lucotti, A.; Pedeferri, M.; Diamanti, M. V. Heterostructured $TiO_2/SiO_2/\gamma$-Fe_2O_3/rGO coating with highly efficient visible-light-induced self-cleaning properties for metallic artifacts. *ACS Appl. Mater. Interfaces* **2020**, *12* (26), 29671−29683.
(19) Bagherzadeh, M.; Kaveh, R.; Mahmoudi, H. Facile synthesis of a recyclable Pd-rGO/CNT/$CaFe_2O_4$ nanocomposite with high multifunctional photocatalytic activity under visible light irradiation. *J. Mater. Chem. A* **2019**, *7* (27), 16257−16266.
(20) Abazari, R.; Mahjoub, A. R.; Salehi, G. Preparation of amine functionalized g-C_3N_4@ H/SMOF NCs with visible light photocatalytic characteristic for 4-nitrophenol degradation from aqueous solution. *J. Hazard. Mater.* **2019**, *365*, 921−931.
(21) Yang, Z.-z.; Zhang, C.; Zeng, G.-m.; Tan, X.-f.; Wang, H.; Huang, D.-l.; Yang, K.-h.; Wei, J.-j.; Ma, C.; Nie, K. Design and engineering of layered double hydroxide based catalysts for water depollution by advanced oxidation processes: a review. *J. Mater. Chem. A* **2020**, *8* (8), 4141−4173.
(22) Kanakaraju, D.; Glass, B. D.; Oelgemöller, M. Advanced oxidation process-mediated removal of pharmaceuticals from water: a review. *J. Environ. Manage.* **2018**, *219*, 189−207.
(23) Bessaha, H.; Harrats, C.; Bouraada, M.; Deménorval, L. C. Photocatalytic efficiency of ZnAl-layered double hydroxide on degradation of a cationic dye under UV and solar radiation. *Chem. Pap.* **2018**, *72* (4), 1031−1040.
(24) Pan, Y.; Abazari, R.; Yao, J.; Gao, J. Recent progress in 2D metal-organic framework photocatalysts: Synthesis, photocatalytic mechanism and applications. *JPhys Energy* **2021**, *3* (3), 032010.
(25) Yan, J.; Zhang, X.; Zheng, W.; Lee, L. Y. S. Interface engineering of a 2D-C_3N_4/NiFe-LDH heterostructure for highly efficient photocatalytic hydrogen evolution. *ACS Appl. Mater. Interfaces* **2021**, *13* (21), 24723−24733.
(26) Li, D.; Zhou, J.; Zhang, Z.; Jiang, Y.; Dong, Z.; Xu, J.; Yao, C. Enhanced photocatalytic activity for CO_2 reduction over a $CsPbBr_3$/CoAl-LDH composite: insight into the S-scheme charge transfer mechanism. *ACS Appl. Energy Mater.* **2022**, *5* (5), 6238−6247.
(27) Sun, C.; Hu, J.; Wu, L.; Xia, Q.; Jiao, F. Construction of a Novel Visible-Light-Driven Z-Scheme NiAl-LDH Modified $(BiO)_2CO_3$ Heterostructure for Enhanced Photocatalytic Degradation Antibiotics Performance in Natural Water Bodies. *Ind. Eng. Chem. Res.* **2023**, *62* (1), 466−477.
(28) Manea, Y. K.; Khan, A. M.; Wani, A. A.; Saleh, M. A.; Qashqoosh, M. T.; Shahadat, M.; Rezakazemi, M. In-grown flower like Al-Li/Th-LDH@ CNT nanocomposite for enhanced photocatalytic degradation of MG dye and selective adsorption of Cr (VI). *J. Environ. Chem. Eng.* **2022**, *10* (1), 106848.
(29) Jo, W.-K.; Tonda, S. Novel CoAl-LDH/g-C_3N_4/RGO ternary heterojunction with notable 2D/2D/2D configuration for highly efficient visible-light-induced photocatalytic elimination of dye and antibiotic pollutants. *J. Hazard. Mater.* **2019**, *368*, 778−787.
(30) Xue, L.; Lü, Z.; Cheng, Y.; Sun, X.; Lin, H.; Xiao, X.; Liu, X.; Zhuo, S. Three-dimensional layered double hydroxide membranes: fabrication technique, growth mechanism, and enhanced photocatalytic activity. *Chem. Commun.* **2018**, *54* (61), 8494−8497.
(31) Sanati, S.; Rezvani, Z.; Abazari, R.; Hou, Z.; Dai, H. Hierarchical CuAl-layered double hydroxide/CoWO 4 nanocomposites with enhanced efficiency for use in supercapacitors with long cycling stability. *New J. Chem.* **2019**, *43* (38), 15240−15248.
(32) Zhao, S.; Liang, Q.; Gao, W.; Zhou, M.; Yao, C.; Xu, S.; Li, Z. In situ growth of $ZnIn_2S_4$ on MOF-derived Ni-Fe LDH to construct ternary-shelled nanotubes for efficient photocatalytic hydrogen evolution. *Inorg. Chem.* **2021**, *60* (13), 9762−9772.
(33) Pan, Y.; Sanati, S.; Abazari, R.; Noveiri, V. N.; Gao, J.; Kirillov, A. M. Pillared-MOF@ NiV-LDH composite as a remarkable electrocatalyst for water oxidation. *Inorg. Chem.* **2022**, *61* (51), 20913−20922.
(34) Sahoo, D. P.; Patnaik, S.; Parida, K. Construction of a Z-scheme dictated WO_3-X/Ag/ZnCr LDH synergistically visible light-induced photocatalyst towards tetracycline degradation and H2 evolution. *ACS Omega* **2019**, *4* (12), 14721−14741.
(35) Shen, R.; Zhang, L.; Li, N.; Lou, Z.; Ma, T.; Zhang, P.; Li, Y.; Li, X. W-N bonds precisely boost Z-scheme interfacial charge transfer in g-C_3N_4/WO_3 heterojunctions for enhanced photocatalytic H2 evolution. *ACS Catal.* **2022**, *12* (16), 9994−10003.
(36) Wang, X.; Maeda, K.; Thomas, A.; Takanabe, K.; Xin, G.; Carlsson, J. M.; Domen, K.; Antonietti, M. A metal-free polymeric photocatalyst for hydrogen production from water under visible light. *Nat. Mater.* **2009**, *8* (1), 76−80.
(37) Sun, H.; Park, S.-J. Bimetallic CuPd nanoparticle-decorated MgAl-LDH/g-C_3N_4 composites for efficient photocatalytic reduction of aqueous Cr (VI). *J. Ind. Eng. Chem.* **2022**, *111*, 183−191.
(38) Yang, M.; Wang, P.; Li, Y.; Tang, S.; Lin, X.; Zhang, H.; Zhu, Z.; Chen, F. Graphene aerogel-based NiAl-LDH/g-C_3N_4 with ultratight sheet-sheet heterojunction for excellent visible-light photocatalytic activity of CO_2 reduction. *Appl. Catal., B* **2022**, *306*, 121065.
(39) Salehi, G.; Abazari, R.; Mahjoub, A. R. Visible-light-induced graphitic-C_3N_4@ nickel-aluminum layered double hydroxide nano-

https://doi.org/10.1021/acsomega.3c07326
ACS Omega 2024, 9, 4581−4593

composites with enhanced photocatalytic activity for removal of dyes in water. *Inorg. Chem.* **2018**, *57* (14), 8681−8691.
(40) Nayak, S.; Parida, K. Dynamics of charge-transfer behavior in a plasmon-induced quasi-type-II p-n/n-n dual heterojunction in Ag@ Ag_3PO_4/g-C_3N_4/NiFe LDH nanocomposites for photocatalytic Cr (VI) reduction and phenol oxidation. *ACS Omega* **2018**, *3* (7), 7324−7343.
(41) Sun, D.; Zhang, Y.; Liu, Y.; Wang, Z.; Chen, X.; Meng, Z.; Kang, S.; Zheng, Y.; Cui, L.; Chen, M.; et al. In-situ homodispersely immobilization of Ag@ AgCl on chloridized g-C_3N_4 nanosheets as an ultrastable plasmonic photocatalyst. *Chem. Eng. J.* **2020**, *384*, 123259.
(42) Mohanty, S.; Babu, P.; Parida, K.; Naik, B. Surface-plasmon-resonance-induced photocatalysis by core-shell SiO_2@ Ag NCs@ Ag_3PO_4 toward water-splitting and phenol oxidation reactions. *Inorg. Chem.* **2019**, *58* (15), 9643−9654.
(43) Su, F.; Li, P.; Huang, J.; Gu, M.; Liu, Z.; Xu, Y. Photocatalytic degradation of organic dye and tetracycline by ternary Ag_2O/AgBr-CeO_2 photocatalyst under visible-light irradiation. *Sci. Rep.* **2021**, *11* (1), 85.
(44) Liang, Y.; Shang, R.; Lu, J.; Liu, L.; Hu, J.; Cui, W. Ag_3PO_4@ UMOFNs core-shell structure: two-dimensional MOFs promoted photoinduced charge separation and photocatalysis. *ACS Appl. Mater. Interfaces* **2018**, *10* (10), 8758−8769.
(45) Garg, R.; Mondal, S.; Sahoo, L.; Vinod, C.; Gautam, U. K. Nanocrystalline Ag_3PO_4 for sunlight-and ambient air-driven oxidation of amines: high photocatalytic efficiency and a facile catalyst regeneration strategy. *ACS Appl. Mater. Interfaces* **2020**, *12* (26), 29324−29334.
(46) Rabiee, N.; Bagherzadeh, M.; Ghadiri, A. M.; Salehi, G.; Fatahi, Y.; Dinarvand, R. ZnAl nano layered double hydroxides for dual functional CRISPR/Cas9 delivery and enhanced green fluorescence protein biosensor. *Sci. Rep.* **2020**, *10* (1), 20672.
(47) Kiani, M.; Bagherzadeh, M.; Fatahi, Y.; Daneshgar, H.; Safarkhani, M.; Salehi, G.; Makvandi, P.; Saeb, M. R.; Lima, E. C.; Rabiee, N. Successive cytotoxicity control by evolutionary surface decorated electronic push-pull green ZnCr-LDH nanostructures: Drug delivery enlargement for targeted breast cancer chemotherapy. *OpenNano* **2022**, *8*, 100093.
(48) Tao, R.; Yang, S.; Shao, C.; Li, X.; Li, X.; Liu, S.; Zhang, J.; Liu, Y. Reusable and flexible g-C_3N_4/Ag_3PO_4/polyacrylonitrile heterojunction nanofibers for photocatalytic dye degradation and oxygen evolution. *ACS Appl. Nano Mater.* **2019**, *2* (5), 3081−3090.
(49) Wang, L.; Li, Y.; Zhang, C.; Deng, D.; He, H.; Yan, X.; Li, Z.; Luo, L. Hierarchical NiMn layered double hydroxide nanostructures on carbon cloth for electrochemical detection of hydrogen peroxide. *ACS Appl. Nano Mater.* **2022**, *5* (12), 17741−17749.
(50) Mehtab, A.; Alshehri, S. M.; Ahmad, T. Photocatalytic and photoelectrocatalytic water splitting by porous g-C_3N_4 nanosheets for hydrogen generation. *ACS Appl. Nano Mater.* **2022**, *5* (9), 12656−12665.
(51) Kumar, S.; Surendar, T.; Baruah, A.; Shanker, V. Synthesis of a novel and stable gC_3N_4-Ag_3PO_4 hybrid nanocomposite photocatalyst and study of the photocatalytic activity under visible light irradiation. *J. Mater. Chem. A* **2013**, *1* (17), 5333−5340.
(52) Chen, C.-R.; Zeng, H.-Y.; Xiong, J.; An, D.-S.; Li, S. Multiple Hierarchical Heterojunction g-C_3N_4/LDH/Ag_3PO_4 with Enhanced Visible-Light Photocatalytic Activity for Cr (VI) Reduction. *Clays Clay Miner.* **2021**, *69* (2), 243−253.
(53) Bai, S.; Wang, Z.; Tan, L.; Waterhouse, G. I.; Zhao, Y.; Song, Y.-F. 600 nm irradiation-induced efficient photocatalytic CO_2 reduction by ultrathin layered double hydroxide nanosheets. *Ind. Eng. Chem. Res.* **2020**, *59* (13), 5848−5857.
(54) Nayak, S.; Mohapatra, L.; Parida, K. Visible light-driven novel gC_3N_4/NiFe-LDH composite photocatalyst with enhanced photocatalytic activity towards water oxidation and reduction reaction. *J. Mater. Chem. A* **2015**, *3* (36), 18622−18635.
(55) Landi, S.; Segundo, I. R.; Freitas, E.; Vasilevskiy, M.; Carneiro, J.; Tavares, C. J. Use and misuse of the Kubelka-Munk function to obtain the band gap energy from diffuse reflectance measurements. *Solid State Commun.* **2022**, *341*, 114573.
(56) Clavero, C. Plasmon-induced hot-electron generation at nanoparticle/metal-oxide interfaces for photovoltaic and photocatalytic devices. *Nat. Photonics* **2014**, *8* (2), 95−103.
(57) Han, C.; Chen, Z.; Zhang, N.; Colmenares, J. C.; Xu, Y. J. Hierarchically CdS decorated 1D ZnO nanorods-2D graphene hybrids: low temperature synthesis and enhanced photocatalytic performance. *Adv. Funct. Mater.* **2015**, *25* (2), 221−229.
(58) Yue, Z.; Liu, A.; Zhang, C.; Huang, J.; Zhu, M.; Du, Y.; Yang, P. Noble-metal-free hetero-structural CdS/Nb_2O_5/N-doped-graphene ternary photocatalytic system as visible-light-driven photocatalyst for hydrogen evolution. *Appl. Catal., B* **2017**, *201*, 202−210.
(59) Peng, L.; Yu, C.; Ma, Y.; Xie, G.; Xie, X.; Wu, Z.; Zhang, N. Self-assembled transition metal chalcogenides@ CoAl-LDH 2D/2D heterostructures with enhanced photoactivity for hydrogen evolution. *Inorg. Chem. Front.* **2022**, *9* (5), 994−1005.
(60) Ye, X.; Chen, Y.; Ling, C.; Zhang, J.; Meng, S.; Fu, X.; Wang, X.; Chen, S. Chalcogenide photocatalysts for selective oxidation of aromatic alcohols to aldehydes using O_2 and visible light: A case study of $CdIn_2S_4$, CdS and In_2S_3. *Chem. Eng. J.* **2018**, *348*, 966−977.
(61) Huang, H.; Jiang, X.; Li, N.; Chen, D.; Xu, Q.; Li, H.; He, J.; Lu, J. Noble-metal-free ultrathin MXene coupled with In_2S_3 nanoflakes for ultrafast photocatalytic reduction of hexavalent chromium. *Appl. Catal., B* **2021**, *284*, 119754.
(62) Kumar, A.; Samanta, S.; Srivastava, R. Systematic investigation for the photocatalytic applications of carbon nitride/porous zeolite heterojunction. *ACS Omega* **2018**, *3* (12), 17261−17275.
(63) Yang, M.-Q.; Xu, Y.-J.; Lu, W.; Zeng, K.; Zhu, H.; Xu, Q.-H.; Ho, G. W. Self-surface charge exfoliation and electrostatically coordinated 2D hetero-layered hybrids. *Nat. Commun.* **2017**, *8* (1), 14224.
(64) Nayak, D.; Kumar, A.; Thangavel, R. Synthesis of MoS_2 Nanoflowers for Photocatalytic Degradation of Organic Dyes. *ACS Appl. Nano Mater.* **2023**, *6* (20), 19476−19490.
(65) Ben Naceur, J.; Ouertani, R.; Chakhari, W.; Chtourou, R. Photo-electrochemical properties of Sb_2S_3/TiO_2 heterostructures integrally synthesis by hydrothermal method. *J. Mater. Sci. Mater. Electron.* **2019**, *30*, 5631−5639.
(66) Elbakkay, M. H.; El Rouby, W. M.; El-Dek, S.; Farghali, A. A. S-TiO_2/S-reduced graphene oxide for enhanced photoelectrochemical water splitting. *Appl. Surf. Sci.* **2018**, *439*, 1088−1102.
(67) Elbakkay, M. H.; El Rouby, W. M.; Mariño-López, A.; Sousa-Castillo, A.; Salgueirino, V.; El-Dek, S.; Farghali, A. A.; Correa-Duarte, M. A.; Millet, P. One-pot synthesis of TiO_2/Sb_2S_3/RGO complex multicomponent heterostructures for highly enhanced photoelectrochemical water splitting. *Int. J. Hydrogen Energy* **2021**, *46* (61), 31216−31227.
(68) Takanabe, K. Photocatalytic water splitting: quantitative approaches toward photocatalyst by design. *ACS Catal.* **2017**, *7* (11), 8006−8022.
(69) Akintunde, O. O.; Yu, L.; Hu, J.; Kibria, M. G.; Achari, G. Visible-light driven photocatalytic degradation of 4-chlorophenol using graphitic carbon nitride-based nanocomposites. *Catalysts* **2022**, *12* (3), 281.
(70) Wang, K.; Li, J.; Zhang, G. Ag-bridged Z-scheme 2D/2D $Bi_5FeTi_3O_{15}$/g-C_3N_4 heterojunction for enhanced photocatalysis: mediator-induced interfacial charge transfer and mechanism insights. *ACS Appl. Mater. Interfaces* **2019**, *11* (31), 27686−27696.

https://doi.org/10.1021/acsomega.3c07326
ACS Omega 2024, 9, 4581−4593